

# Research on Resistive Switching and Synaptic Performance of $\text{CeO}_x/\text{TaO}_x$ -Based Memristor

Xinrong Ren, Yuede Nan, Xu Chen, Ruyun Ding, and Hui Zheng\*

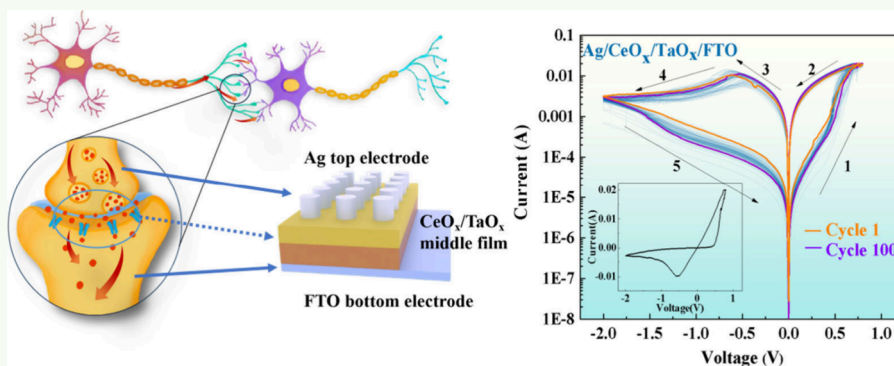
Cite This: <https://doi.org/10.1021/acsaelm.5c00483>

Read Online

ACCESS |

Metrics &amp; More

Article Recommendations



**ABSTRACT:** Dual-terminal memristors have emerged as pivotal candidates for next-generation nonvolatile memory due to their fast switching and low energy consumption. In this study, we fabricated  $\text{Ag}/\text{CeO}_x/\text{TaO}_x/\text{FTO}$  and  $\text{Ag}/\text{TaO}_x/\text{FTO}$  memristors and systematically investigated their resistive switching behaviors and synaptic functionalities. The incorporation of a  $\text{CeO}_x$  interlayer significantly enhances oxygen vacancy concentration, reduces the SET/RESET voltages ( $0.55\text{ V}/-2\text{ V}$  vs  $2\text{ V}/-3\text{ V}$  for  $\text{Ag}/\text{TaO}_x/\text{FTO}$ ), and broadens the memory window (resistance ratio  $>100$ ). Moreover, the  $\text{CeO}_x$  layer stabilizes oxygen vacancy migration, achieving excellent endurance ( $>1000$  cycles) and retention stability ( $\text{CV} < 17\%$  over  $10^4\text{ s}$ ). Notably, the device emulates synaptic plasticity, including long-term potentiation/depression (LTP/LTD), spike-timing-dependent plasticity (STDP), and paired-pulse facilitation (PPF), with high linearity. These advancements position the  $\text{Ag}/\text{CeO}_x/\text{TaO}_x/\text{FTO}$  memristor as a promising platform for energy-efficient neuromorphic computing.

**KEYWORDS:** Memristor, oxygen vacancy, synaptic plasticity, neural network,  $\text{CeO}_x$  low-voltage operation

## INTRODUCTION

In recent years, the dual-terminal memristor has garnered significant attention, and is anticipated to become a pivotal device for the next generation of nonvolatile memory.<sup>1–3</sup> Based on a straightforward metal/insulator/metal (MIM) dual-terminal design, the memristor is capable of switching between a high resistance state (HRS) and a low resistance state (LRS) through electric field-induced formation/dissolution of conductive filaments (CFs). When the voltage exceeds the threshold voltage ( $V_{\text{set}}$ ), CFs nucleate to establish a conductive pathway, enabling a rapid transition to LRS (SET state). Conversely, applying a reverse reset voltage ( $V_{\text{reset}}$ ) disrupts the CFs, restoring the HRS (RESET state). Its advantages encompass extremely fast running speed, three-dimensional storage options, large data storage capacity, multilayer storage capacity and minimum energy usage.<sup>4–6</sup> In addition, as research into artificial neural networks deepens, the use of memristors to simulate artificial synapses and neurons has become a prominent topic.<sup>7–9</sup> These memristors are anticipated to achieve uniform conductance modulation

under pulse sequence stimulation, thereby simplifying the weight updating process of neural networks and hardware circuits. Furthermore, high-precision pattern recognition can also be obtained through the linear conductance weights generated by the enhanced/inhibitory behavior of the device to train the neural network.

Among the various materials used to prepare memristors—such as binary oxides, ferrites, organic compounds, and sulfides<sup>10–15</sup>—a widely accepted theoretical model for the resistance mechanism of oxide memristors is the oxygen vacancy conduction mechanism. In oxides where oxygen vacancies are the primary resistive switching mechanism,

**Received:** March 10, 2025

**Revised:** May 11, 2025

**Accepted:** May 15, 2025

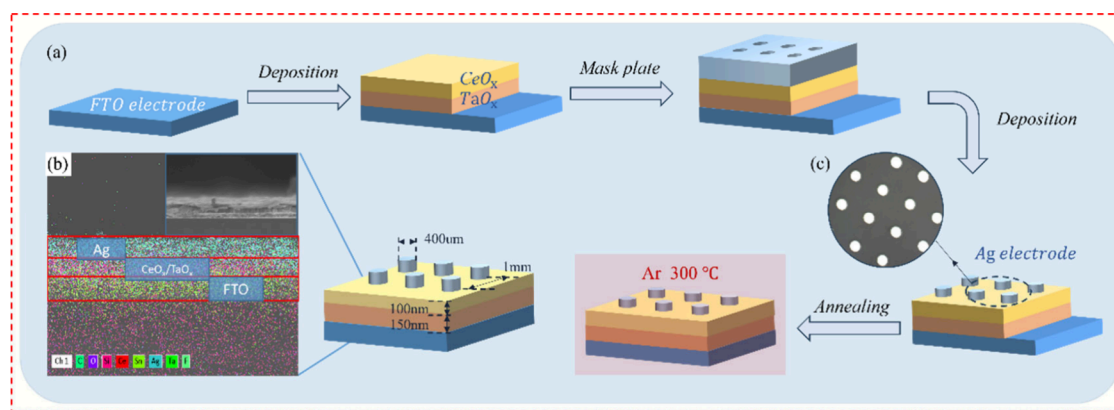


**Figure 1.** (a) Preparation process of Ag/CeO<sub>x</sub>/TaO<sub>x</sub>/FTO film. (b) EDS spectrum, SEM cross-sectional image and 3D schematic diagram of the Ag/CeO<sub>x</sub>/TaO<sub>x</sub>/FTO thin film in the illustration. (c) Top electrode lattice under microscope.

TaO<sub>x</sub> and CeO<sub>x</sub> are considered ideal intermediate layer materials.<sup>16,17</sup> The valence variation of the Ta element in Tantalum oxide (TaO<sub>x</sub>) materials is minimal, resulting in a long switching life and high write speed.<sup>18–20</sup> Cerium oxide (CeO<sub>x</sub>), with its narrow bandgap (2.7 eV) and high oxygen storage capacity, facilitates oxygen vacancies (V<sub>o</sub><sup>2+</sup>) generation and migration. Theoretical calculations indicate that the lower Ce–O bond energy promotes V<sub>o</sub><sup>2+</sup> redistribution under electric fields. Consequently, CeO<sub>x</sub> exhibits good write speed, multilevel storage characteristics, and low switching voltage.<sup>21,22</sup> Furthermore, most memristors fail to achieve long-term potentiation and depression due to the randomness and instability of the conductive pathways formed by oxygen vacancies.<sup>23</sup> The improved switching behavior in multilayer structures is attributed to the control of oxygen vacancy motion within the dielectric layers and at the interfaces,<sup>24–26</sup> which further reduces the operating voltage and power consumption of the device. Consequently, many bilayer<sup>27–29</sup> and trilayer<sup>30,31</sup> topologies have been proposed to enhance the resistive switching performance of these devices.

In this study, Ag/CeO<sub>x</sub>/TaO<sub>x</sub>/FTO and Ag/TaO<sub>x</sub>/FTO composite thin-film memristors were fabricated. The Ag/TaO<sub>x</sub>/FTO memristor demonstrated clear memristive behavior, featuring a relatively large memory window and the ability to retain obvious memristive characteristics after 1000 cycles. More interestingly, the cerium oxide layer was introduced in the Ag/CeO<sub>x</sub>/TaO<sub>x</sub>/FTO memristor to control the movement of oxygen vacancies at the interface and within the oxide layers. This modification resulted in a reduction of the switching voltage, thereby lowering energy consumption, expanding the memory window, and enhancing stability and resistance retention. Consequently, the device demonstrates improved performance for applications in nonvolatile memory. Furthermore, we discuss the reasons behind the performance improvements attributed to the CeO<sub>x</sub> layer, offering a potential solution for further enhancing device performance. Additionally, due to the continuous resistance change during the switching process, Ag/CeO<sub>x</sub>/TaO<sub>x</sub>/FTO composite memristor devices exhibit excellent synaptic properties, including long-term potentiation (LTP), long-term depression (LTD), spike-timing-dependent plasticity (STDP), and paired-pulse facilitation (PPF). These characteristics make them highly suitable for applications in neural networks.

## EXPERIMENTAL SECTION

The process of preparing the Ag/CeO<sub>x</sub>/TaO<sub>x</sub>/FTO composite film and testing its memristive properties is illustrated in Figure 1(a). Initially, the TaO<sub>x</sub> film was deposited on the FTO electrode (500 nm, purchased from Xiangcheng Company) using electron beam evaporation at a deposition rate of approximately 0.3–0.6 Å/s, achieving a thickness of 150 nm. Subsequently, the CeO<sub>x</sub> film was deposited onto the TaO<sub>x</sub> layer via electron beam evaporation, at a deposition rate of approximately 0.6–0.8 Å/s and to a thickness of 100 nm. Finally, the Ag electrode was deposited on the CeO<sub>x</sub> layer using the same method but at the deposition rate of 1–1.5 Å/s and to a thickness of 200 nm. The deposition parameters are detailed in Table 1. The resulting Ag/CeO<sub>x</sub>/TaO<sub>x</sub>/FTO composite films were

**Table 1.** Deposition conditions of the Ag, CeO<sub>x</sub>, and TaO<sub>x</sub> films

	Ag	CeO <sub>x</sub>	TaO <sub>x</sub>
Base pressure	$5 \times 10^{-4}$ Pa	$5 \times 10^{-4}$ Pa	$5 \times 10^{-4}$ Pa
Beam current	55 mA	30 mA	60 mA
Sedimentation rate	1–1.5 Å/s	0.6–0.8 Å/s	0.3–0.6 Å/s
Film thickness	~200 nm	~100 nm	~150 nm

then annealed at 300 °C for 30 min under atmospheric pressure in Ar gas. The high oxygen vacancy concentration in CeO<sub>x</sub> leads to poor performance dispersion of the devices. Annealing can increase the grain size in the films and reduce the oxygen vacancy concentration in CeO<sub>x</sub> and TaO<sub>x</sub> films, thereby decreasing the dispersion of V<sub>SET</sub>, V<sub>RESET</sub>, R<sub>LRS</sub>, and R<sub>HRS</sub> in Ag/CeO<sub>x</sub>/TaO<sub>x</sub>/FTO devices.

The microstructure and morphology of the Ag/CeO<sub>x</sub>/TaO<sub>x</sub>/FTO composite films were analyzed using X-ray diffraction (XRD, Ultima IV) and field emission scanning electron microscopy (SEM, JSM-7800F). The chemical states of the films were characterized by X-ray photoemission spectroscopy (XPS, ESCALab250, USA) and energy-dispersive spectroscopy (EDS, Xplore15). The resistance switching performance of the device was evaluated at room temperature using a Keithley 4200 instrument. The I–V curves of the memristor were measured by applying a triangular DC voltage sweep with maximum amplitudes ranging from ± 0.5 V to ± 5 V, reflecting the resistive switching characteristics, including the high-to-low resistance ratio, reproducibility, and variation rate. The retention characteristics of the memristor were assessed by applying a read voltage of 0.15 V at 1-s intervals over 10000 s under specific configurations. Additionally, the synaptic properties of the memristor, including long-term potentiation (LTP), long-term depression (LTD), spike-timing-dependent plasticity (STDP), and paired-pulse facilitation (PPF), were tested by applying pulse voltages of varying amplitudes, pulse widths, and intervals.

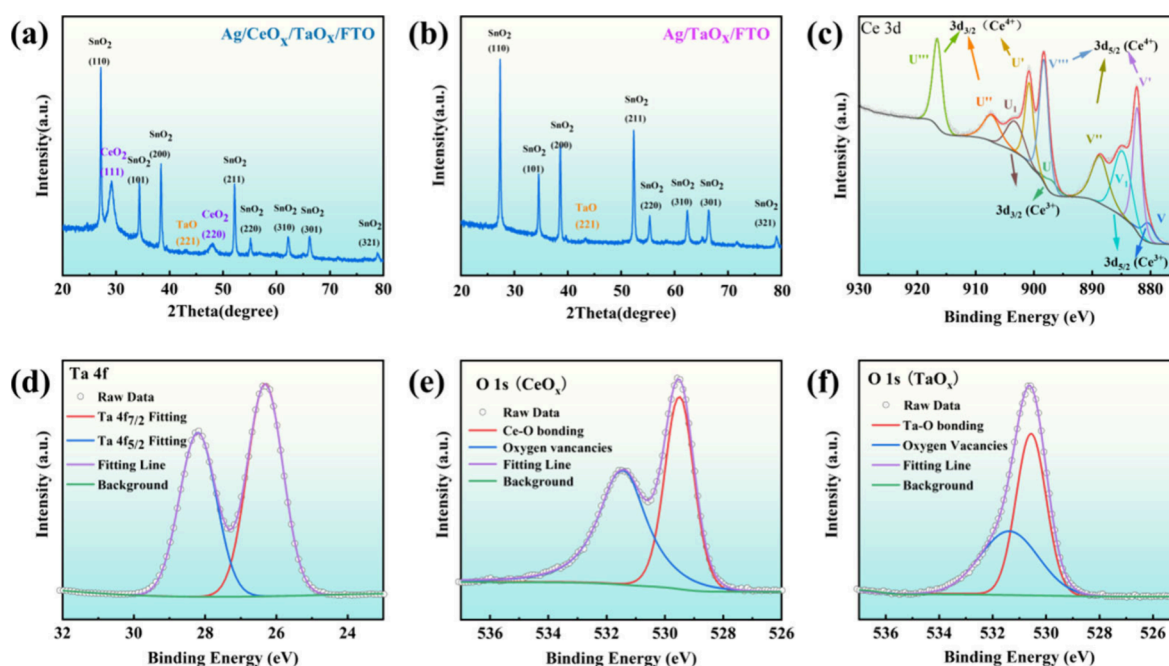


**Figure 2.** (a) XRD pattern of the Ag/CeO<sub>x</sub>/TaO<sub>x</sub>/FTO composite films. (b) XRD pattern of the Ag/TaO<sub>x</sub>/FTO composite films. (c) High resolution of Ce 3d spectrum. (d) High resolution of O 1s spectrum of the CeO<sub>x</sub>. (e) High resolution of Ta 4f spectrum. (f) High resolution of O 1s spectrum of the TaO<sub>x</sub>.

## 2. RESULTS AND DISCUSSION

Figure 1(a) illustrates the preparation process of the Ag/CeO<sub>x</sub>/TaO<sub>x</sub>/FTO composite film. TaO<sub>x</sub> and CeO<sub>x</sub> thin films were sequentially deposited on the FTO electrode, followed by the deposition of Ag electrodes through a mask to create discrete silver dot arrays. A test voltage was then applied between the exposed FTO electrode and the Ag top electrode to evaluate the memristive properties of the thin films.

Figure 1(b) in the set shows the cross-section of Ag/CeO<sub>x</sub>/TaO<sub>x</sub>/FTO under the electron microscope, revealing clear stratification between the TaO<sub>x</sub> and CeO<sub>x</sub> intermediate layers and the FTO bottom layer, including the distinct layered structure between the metal electrode and the oxide layer. Figure 1(b) illustrates the distribution of elements in the Ag/CeO<sub>x</sub>/TaO<sub>x</sub>/FTO cross-section, where Ag elements are concentrated at the top layer, and Sn, Ta, and Ce elements exhibit clear hierarchical characteristics. Figure 1(c) shows that, under the microscope, the small metal cylinders of Ag are evenly distributed on the oxide layer, serving as electrodes. Each Ag electrode is approximately 400 μm in diameter, with an interval of about 1 mm between them.

Many studies have shown that the memristive properties of binary oxide memristors are related to oxygen vacancies and the valence state of metal elements.<sup>32–34</sup> Therefore, further analysis was conducted on the crystal structure of the composite films. Figure 2(a) and (b) shows XRD patterns of the Ag/CeO<sub>x</sub>/TaO<sub>x</sub>/FTO and Ag/TaO<sub>x</sub>/FTO films annealed at 300 °C, respectively. It can be observed that the TaO<sub>x</sub> oxide layer in the Ag/TaO<sub>x</sub>/FTO film exhibits growth along the TaO (221) plane. Additionally, in the Ag/CeO<sub>x</sub>/TaO<sub>x</sub>/FTO film, besides the TaO planes, there are also CeO<sub>2</sub> (111) and (220) planes, indicating partial crystallization in both the CeO<sub>x</sub> and TaO<sub>x</sub> layers. Figure 2(c–f) shows the XPS profiles of the Ce, Ta, and O elements in the Ag/CeO<sub>x</sub>/TaO<sub>x</sub>/FTO films. The XPS profile of the cerium element on the 3d track is shown in Figure 2(c). A total of 10 peaks were extracted by

deconvolution from this XPS spectrum, with four peaks attributed to Ce<sup>3+</sup> and the remaining six peaks attributed to Ce<sup>4+</sup>. Peaks belonging to Ce<sup>3+</sup> are labeled as U<sub>1</sub>, U, V<sub>1</sub>, V, while peaks belonging to Ce<sup>4+</sup> are labeled as U<sup>'''</sup>, U<sup>''</sup>, U', V<sup>'''</sup>, V<sup>''</sup>, V'.<sup>35</sup> To distinguish characteristic peaks on different tracks, peaks labeled 'U' indicate electrons on Ce 3d<sub>3/2</sub> and peaks labeled 'V' indicate electrons on Ce 3d<sub>5/2</sub>. Previous studies have shown that the reduction of Ce<sup>4+</sup> to Ce<sup>3+</sup> leads to the formation of oxygen vacancies.<sup>36</sup> The proportion of Ce<sup>3+</sup> atoms relative to the total amount of Ce is generally related to the surface oxygen vacancy content. The ratio of the summed area of all Ce<sup>3+</sup> peaks to the total peak area of Ce<sup>4+</sup> determines the Ce<sup>3+</sup> content, which in this case is 28.41%.<sup>37</sup>

Figure 2(d) shows the XPS spectrum of Ta elements on the 4f track, with two peaks corresponding to the 4f<sub>5/2</sub> and 4f<sub>7/2</sub> orbitals at binding energies of 28.20 and 26.31 eV, respectively. Figure 2(e) and (f) shows the XPS spectra of oxygen elements on the O 1s track for the CeO<sub>x</sub> and TaO<sub>x</sub> layers, respectively. In Figure 2(e), corresponding to CeO<sub>x</sub>, the small peak at 532.2 eV corresponds to chemisorbed oxygen, which can be attributed to the lower binding energies of fully oxidized CeO<sub>x</sub> compared to its oxygen-deficient counterpart.<sup>38</sup> The lattice oxygen (O<sub>L</sub>) in the CeO<sub>x</sub> and TaO<sub>x</sub> layers appears at 529.43 and 530.56 eV, respectively, indicating Ce–O and Ta–O bonding, while the oxygen vacancy (O<sub>V</sub>) is positioned at 531.34 eV. The lower bond energy of Ce–O implies that oxygen vacancies in the CeO<sub>x</sub> layer can more easily migrate and redistribute under external energy influences such as electric fields or thermal excitation, and potentially transfer to the TaO<sub>x</sub> layer. Additionally, the oxygen vacancy content (O<sub>V</sub>/(O<sub>V</sub> + O<sub>L</sub>)) in the CeO<sub>x</sub> and TaO<sub>x</sub> layers is 53.76% and 43.54%, respectively. This increase in oxygen vacancy content and the change in tantalum valence ratio may play a key role in the transition of memristor resistance.

The I–V characteristic curves for the Ag/CeO<sub>x</sub>/TaO<sub>x</sub>/FTO memristor and the Ag/TaO<sub>x</sub>/FTO memristor over 100 cycles



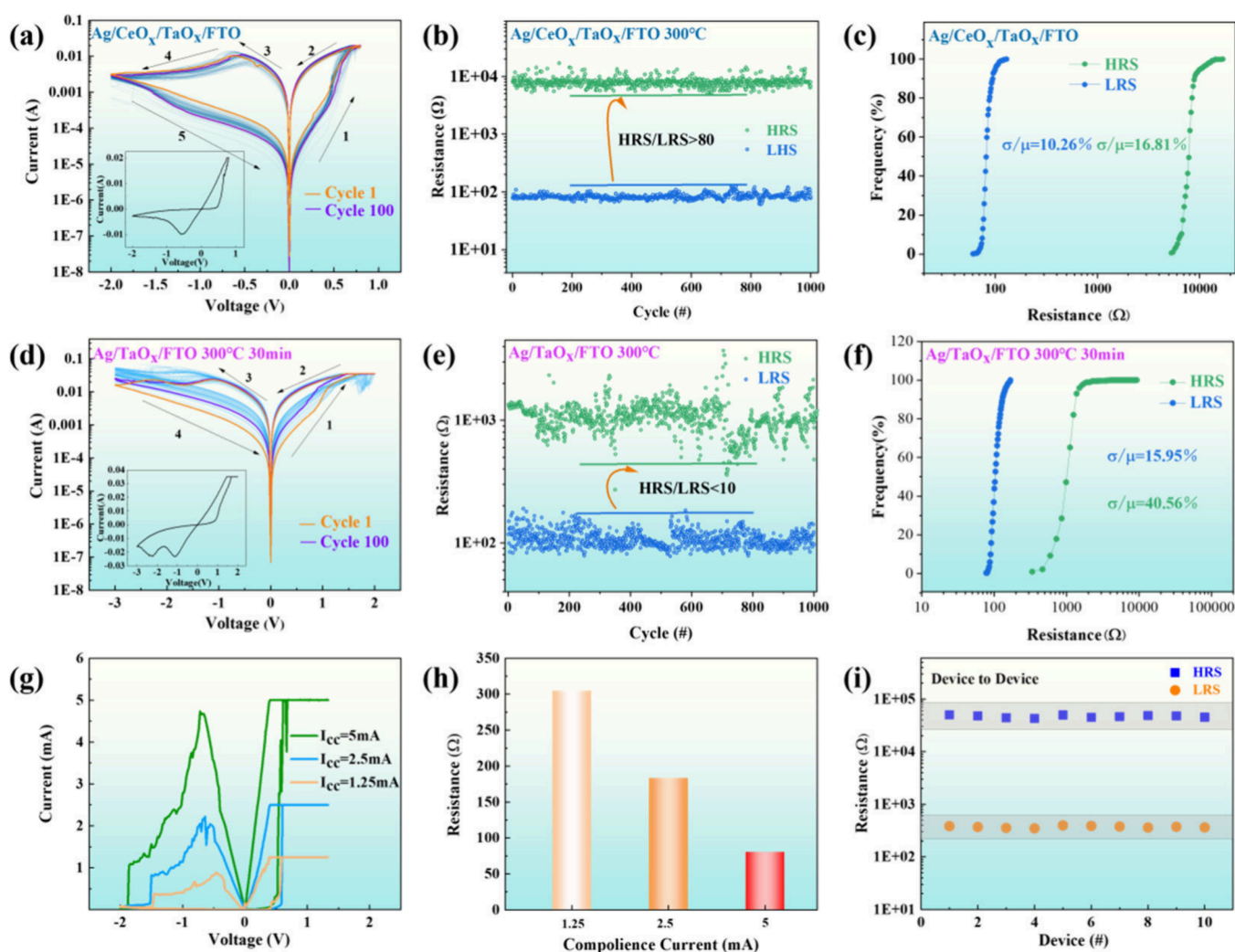


**Figure 3.** (a) 100-cycle curves of the Ag/CeO<sub>x</sub>/TaO<sub>x</sub>/FTO memristors; the Ag/CeO<sub>x</sub>/TaO<sub>x</sub>/FTO memristors single-cycle curves are shown in the inset. (b) Distribution of resistance of Ag/CeO<sub>x</sub>/TaO<sub>x</sub>/FTO memristor in 1000 cycles. (c) Frequency distribution and rate of resistance of Ag/CeO<sub>x</sub>/TaO<sub>x</sub>/FTO memristor in 1000 cycles. (d) 100-cycle curves of the Ag/TaO<sub>x</sub>/FTO memristors; the Ag/TaO<sub>x</sub>/FTO memristors single-cycle curves are shown in the inset. (e) Distribution of resistance of Ag/TaO<sub>x</sub>/FTO memristor in 1000 cycles. (f) Frequency distribution and rate of resistance of Ag/TaO<sub>x</sub>/FTO memristor in 1000 cycles. (g) Ag/CeO<sub>x</sub>/TaO<sub>x</sub>/FTO memristor curves at different compliance currents ( $I_{cc}$ ). (h) Ag/CeO<sub>x</sub>/TaO<sub>x</sub>/FTO low configuration resistance with compliance current  $I_{cc}$ . (i) Distribution of high and low resistance of 10 different memristors.

are presented in Figure 3(a) and (d), respectively. The current values are shown as absolute magnitudes on a logarithmic scale. As illustrated in Figure 3(a), the current initially increases at a steady rate with rising voltage. Upon reaching the threshold voltage, referred to as  $V_{set}$ ,<sup>39</sup> which is approximately 0.55 V for the Ag/CeO<sub>x</sub>/TaO<sub>x</sub>/FTO memristor, a sharp increase in the current slope is observed. This increase causes the current to elevate by one to two orders of magnitude, transitioning the memristor into a low-resistance state (LRS).<sup>40,41</sup> Subsequently, as the voltage is decreased to a specific reverse voltage ( $V_{reset}$ ), the current reduces to zero, indicating a transition to a high-resistance state (HRS).<sup>42</sup> The inset I–V characteristic curves in Figure 3(a) and (d) depict the electrical responses of the Ag/CeO<sub>x</sub>/TaO<sub>x</sub>/FTO and Ag/TaO<sub>x</sub>/FTO memristors over 100 cycles, highlighting significant differences in the switching behaviors of the two devices. During a single operational cycle of scanning voltage on the memristor, the Ag/CeO<sub>x</sub>/TaO<sub>x</sub>/FTO memristor exhibits significantly lower upper/cutoff voltages of 0.8 V and –2 V, respectively, compared to the Ag/TaO<sub>x</sub>/FTO memristor,

which displays higher switching voltages of 2 V and –3 V. This reduction in switching voltages enhances the applicability of the Ag/CeO<sub>x</sub>/TaO<sub>x</sub>/FTO memristor in low-power applications. Furthermore, the Ag/CeO<sub>x</sub>/TaO<sub>x</sub>/FTO memristor demonstrates an increased memory window and a higher high-to-low resistance ratio, suggesting improved stability and performance. According to the resistance distributions analyzed in Figure 3(b) and (e), measured at a read voltage of 0.15 V after 1000 cycles, the Ag/CeO<sub>x</sub>/TaO<sub>x</sub>/FTO memristor shows superior electrical characteristics, potentially offering broader functional capabilities in memristive device applications. The observed resistance ratio characteristics of the Ag/CeO<sub>x</sub>/TaO<sub>x</sub>/FTO memristors indicate a significant improvement over the Ag/TaO<sub>x</sub>/FTO memristors. Specifically, the minimum high-to-low resistance ratio of Ag/CeO<sub>x</sub>/TaO<sub>x</sub>/FTO memristors exceeds 80, with an average ratio above 100. In contrast, the corresponding minimum ratio for Ag/TaO<sub>x</sub>/FTO memristors falls below 10. This data indicates that Ag/CeO<sub>x</sub>/TaO<sub>x</sub>/FTO memristors offer a larger memory window and enhanced accuracy, making them more suitable



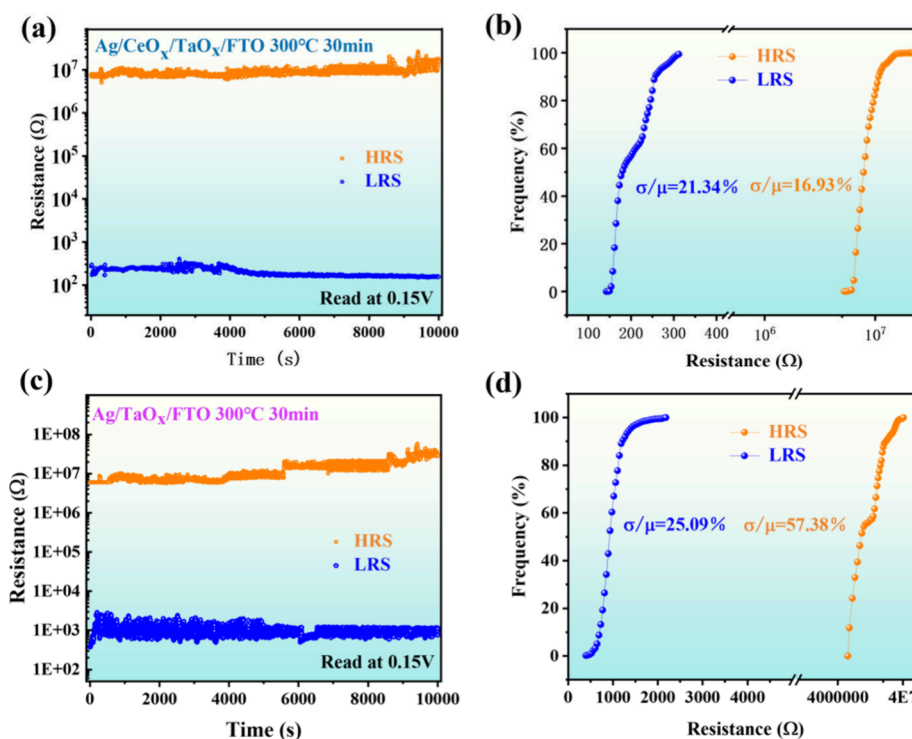


**Figure 4.** Retention curves of high and low resistance read at 0.15 V at 10,000 s (a) for Ag/CeO<sub>x</sub>/TaO<sub>x</sub>/FTO and (c) Ag/TaO<sub>x</sub>/FTO. Frequency distribution of (b) Ag/CeO<sub>x</sub>/TaO<sub>x</sub>/FTO and (d) Ag/TaO<sub>x</sub>/FTO.

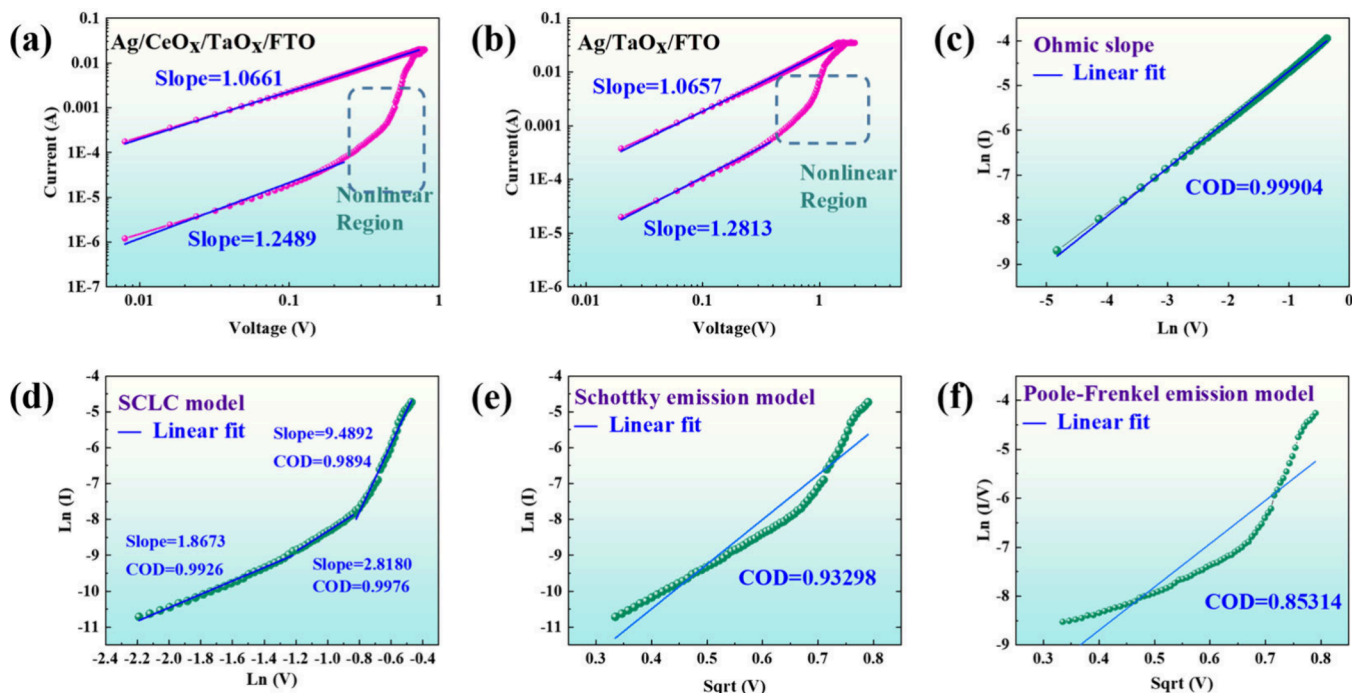


**Figure 5.** Representative current–voltage plots for RS behavior of the memristor devices: (a) Ag/CeO<sub>x</sub>/TaO<sub>x</sub>/FTO and (b) Ag/CeO<sub>x</sub>/TaO<sub>x</sub>/FTO. Ag/CeO<sub>x</sub>/TaO<sub>x</sub>/FTO memristors curve fits the Ohmic model (c) for low resistance and SCLC model (d), Schottky emission model (e), and Poole-Frenkel emission model (f) for high resistance.

for nonvolatile memory applications. Moreover, the reproducibility of the Ag/CeO<sub>x</sub>/TaO<sub>x</sub>/FTO memristor is highlighted by its lower coefficient of variation (CV, the degree of dispersion of resistance distribution, defined as  $\delta/\mu$ , where  $\delta$  is the standard deviation of HRS/LRS and  $\mu$  is the average)<sup>43</sup> in the high resistance state (HRS), recorded at 16.81%, compared

to 40.56% for the Ag/TaO<sub>x</sub>/FTO memristor. This lower CV underscores the stability and reliability of the Ag/CeO<sub>x</sub>/TaO<sub>x</sub>/FTO memristor, enhancing its utility in nonvolatile memory devices.

Figure 3(c) and (f) illustrates the frequency distributions of resistance states for both memristor types, further substantiat-

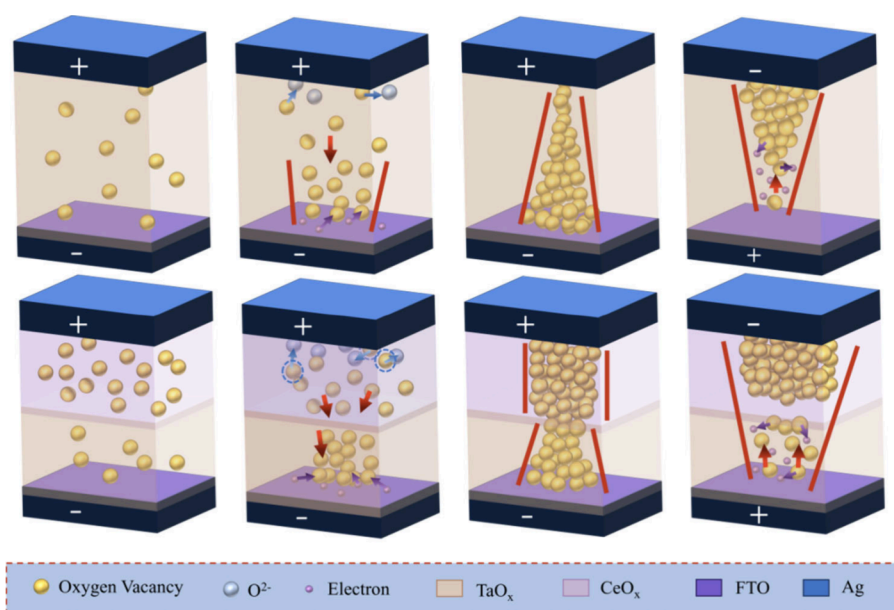


**Figure 6.** Mechanism diagram of Ag/TaO<sub>x</sub>/FTO memristor (upper layer) and Ag/CeO<sub>x</sub>/TaO<sub>x</sub>/FTO memristor (lower layer) based on the oxygen vacancy conduction current model.

ing these findings. Figure 3(g) illustrates the cyclic curves of the Ag/CeO<sub>x</sub>/TaO<sub>x</sub>/FTO memristor under different compliance currents ( $I_{cc}$ ).<sup>44,45</sup> The memristive profile at various current limits generally maintains a stable low-resistance state (LRS), albeit with slight variations in resistance values. The switching voltage remains approximately constant across different settings, indicating robust voltage thresholds for the device. Figure 3(h) analyzes the LRS at a fixed read voltage of 0.15 V for three distinct compliance currents. It is observed that the resistance in LRS decreases as the compliance current increases, suggesting that the resistance level of LRS can be effectively modulated by varying the compliance current. This feature enhances the device's adaptability for different applications by allowing for dynamic resistance adjustments. Furthermore, the device demonstrates excellent spatial uniformity.<sup>46,47</sup> This is evidenced by tests conducted on ten separate devices (Device to Device), with the high-resistance state (HRS) and LRS being documented for each. Figure 3(i) presents the distribution of the high and low resistance values at a compliance current ( $I_{cc}$ ) of 10 mA for these devices. The resistance switch ratio across all devices is closely grouped around a mean of 125.9, with a remarkably low coefficient of variation (CV) at 4.06%. This low variability confirms the memristor's stability and uniform response across multiple devices, underscoring its reliability for consistent performance in practical applications.

Figure 4(a) and (c) displays the resistance retention profiles of the Ag/CeO<sub>x</sub>/TaO<sub>x</sub>/FTO and Ag/TaO<sub>x</sub>/FTO memristors over a duration of 10000 s. Initially, the memristors are switched to a low resistance state (LRS) by applying a forward voltage exceeding the set voltage, followed by a stabilization phase where a read voltage of 0.15 V is applied to monitor resistance changes over the specified period. Subsequently, a negative voltage below the reset threshold reverts the devices to a high resistance state (HRS), with resistance readings taken at 1-s intervals for 10000 s to assess stability. Figure 4(b) and (d) illustrates the resistance variability of both memristor types within the same period. The Ag/CeO<sub>x</sub>/TaO<sub>x</sub>/FTO memristors exhibit coefficients of variation (CV) in high and low

resistance values of 16.93% and 21.34%, respectively, which are notably lower than those observed in the Ag/TaO<sub>x</sub>/FTO memristors. This reduced variability in resistance states suggests that Ag/CeO<sub>x</sub>/TaO<sub>x</sub>/FTO memristors possess superior memory retention characteristics, enhancing their suitability for applications in nonvolatile memory systems and neural network implementations. This performance advantage underscores their potential for reliable, long-term data storage and processing capabilities in advanced computing architectures.

To elucidate the resistance switching mechanisms in Ag/CeO<sub>x</sub>/TaO<sub>x</sub>/FTO and Ag/TaO<sub>x</sub>/FTO memristors, Figure 5(a) and (b) presents the memory resistance curves along with the forward voltage settings for each device type. These curves reveal a linear relationship between voltage and resistance in both the low and high resistance states, characteristic of Ohmic conduction.<sup>48</sup> This linear behavior suggests a straightforward, resistive response to applied voltage changes under normal conditions. However, deviations occur in the high voltage region of the high resistance state (HRS), where the relationship becomes nonlinear. This nonlinearity is further analyzed in Figures 5(c) through (f), which compare the experimental I–V curves with theoretical fits from various conduction models: Space-Charge-Limited Conduction (SCLC),<sup>49</sup> Schottky,<sup>50</sup> and Poole-Frenkel.<sup>51</sup> The coefficient of determination (COD) values accompanying these fits assess the accuracy of each model in describing the experimental data. The data fitting indicates that the Space-Charge-Limited Conduction (SCLC) model is particularly adept at describing the conduction behavior of the Ag/CeO<sub>x</sub>/TaO<sub>x</sub>/FTO memristor under high-voltage and high-resistance conditions. Specifically, the SCLC model shows that in the depicted high resistance region (Figure 5(d)), the initial slope of approximately 1.17 suggests Ohmic conduction at lower voltages, where current conduction is dominated by free charge carriers generated by thermal excitation. As the voltage increases, the slope escalates to 2.37, indicative of a quadratic I–V<sup>2</sup> relationship,<sup>52</sup> and then further increases to 8.79, suggesting trap-filled limit (TFL) conduction<sup>53,54</sup> due to

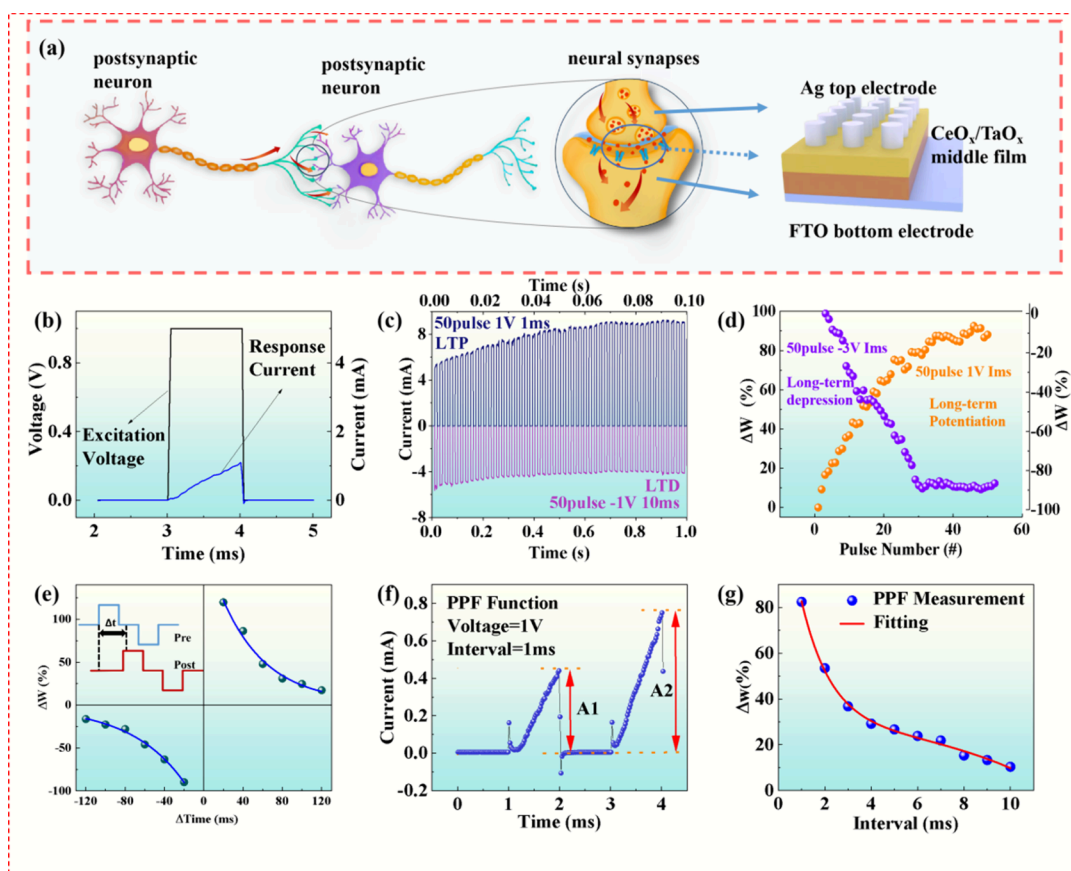


**Figure 7.** (a) Schematic diagram of biological synapse in human brain, which resembles memristive devices with sandwich structure. (b) The response characteristic of the current when applying a pulse voltage of 1 ms pulse width and amplitude of 1 V. (c) Long-term potentiation and depression (LTP, LTD) characteristics of the artificial synapse (blue line: potentiation; black line: depression). The applied pulse voltage signal is 1 V, 1 ms and  $-1$  V, 10 ms. (d) Relationship between pulse number and synaptic weights  $\Delta W$  in LTP/LTD. (e) The STDP characteristics of the memristors; the inset of the figure is the schematic representation of the voltage pulses of the top and bottom electrodes. (f) The current response of the memristor after receiving both anterior and posterior pulses, where the pulse interval is 1 ms. (g) The relation between the synaptic weight changes and the interpulse interval.

deep trap levels within the CeO<sub>x</sub>/TaO<sub>x</sub> film. This steep increase is characteristic of a transition from Ohmic to space-charge-limited current flow, where deep traps significantly impact electron transport. When the voltage is subsequently reduced, the slope decreases back to approximately 0.99 (Figure 5(c)), reaffirming that SCLC predominantly governs the conduction mechanism in the high voltage range of HRS.<sup>55–57</sup>

To better illustrate the memristive mechanism of the Ag/CeO<sub>x</sub>/TaO<sub>x</sub>/FTO memristor and the Ag/TaO<sub>x</sub>/FTO memristor, a schematic of the conductive mechanism based on the oxygen vacancy conduction current model is presented in Figure 6. This phenomenon is attributed to the lower diffusion barrier of oxygen vacancies in the TaO<sub>x</sub> layer compared to that in Ag-based conductive filaments (CFs), where Ag CFs are only partially formed near the Ag/CeO<sub>x</sub> interface.<sup>58–60</sup> In the initial state, oxygen vacancies are randomly distributed in the CeO<sub>x</sub> and TaO<sub>x</sub> layers. When a small positive voltage is applied, lattice oxygen is excited to become oxygen ions and leaves the lattice, forming oxygen vacancies.<sup>61</sup> Simultaneously, the oxygen vacancies between the oxide layers converge due to the forward electric field, forming a conductive filament, though a complete conductive path is not yet established. At this stage, the memristor remains in a high resistance state (HRS), with the current conduction mechanism being

primarily Ohmic. When the voltage exceeds  $V_{set}$ , the conductive filament formed by the oxygen vacancies establishes a complete conductive path. The traps in the oxide layer (most likely oxygen vacancies) are fully filled by carriers, causing a significant increase in current as the memristor transitions to a low resistance state (LRS). In the LRS, current conduction is primarily facilitated by the conductive pathways formed by oxygen vacancies. Upon applying a reverse voltage, the oxygen vacancies migrate toward the top electrode, disrupting the conductive filament and releasing carriers from the traps.<sup>62</sup> Consequently, the memristor reverts to the HRS. Compared to the Ag/TaO<sub>x</sub>/FTO memristor, the cerium oxide layer in the Ag/CeO<sub>x</sub>/TaO<sub>x</sub>/FTO memristor contains a higher concentration of oxygen vacancies and, due to the lower Ce–O bond energy, has a greater tendency to form oxygen vacancies. This higher vacancy concentration facilitates the formation of conductive filaments and pathways, thereby reducing the threshold voltage ( $V_{set}$ ). Furthermore, the Ag/CeO<sub>x</sub>/TaO<sub>x</sub>/FTO memristor exhibits better stability than the Ag/TaO<sub>x</sub>/FTO memristor. This is mainly reflected in the gradual increase of the high resistance current with repeated cycling of the Ag/TaO<sub>x</sub>/FTO memristor. This phenomenon may be attributed to the low mobility of oxygen vacancies in the TaO<sub>x</sub> layer, making the conductive filaments more difficult to disrupt. Additionally, the



higher switching voltage in the Ag/TaO<sub>x</sub>/FTO memristor exacerbates this trend. Therefore, incorporating the CeO<sub>x</sub> layer into the Ag/TaO<sub>x</sub>/FTO structure effectively improves resistive-switching and synaptic characteristics.

In this research, the Ag/CeO<sub>x</sub>/TaO<sub>x</sub>/FTO memristor was demonstrated to effectively simulate the functions of neural synapses in the brain.<sup>63</sup> Figure 7(a) schematically illustrates the fundamental roles of neurons and synapses in the human brain. Neuronal pulses, representing action potentials, are received by presynaptic neurons, leading to the release of neurotransmitters within the synaptic cleft. These neurotransmitters then bind to receptors on the postsynaptic membrane, thereby activating the postsynaptic neuron. To replicate real synaptic functions using a memristive device, the top and bottom electrodes are designated as pre- and postsynaptic channels,<sup>64</sup> respectively. In this model, the device's conductivity serves as an analog for synaptic weight,<sup>65</sup> which can be adjusted through voltage pulses to modulate synaptic plasticity. Synaptic plasticity refers to the synapse's ability to alter its response based on the signals transmitted between neurons, which plays a crucial role in the encoding of neuronal inputs.<sup>66</sup>

Figure 7(b) presents the current response characteristics of the Ag/CeO<sub>x</sub>/TaO<sub>x</sub>/FTO memristor subjected to a pulse voltage of 1 V with a duration of 1 ms.<sup>67</sup> The observed behavior shows a stable and continuous rise in current throughout the application of the voltage. This increase in current can be interpreted as a gradual increase in the memristor's conductance  $G = I/V$  at the given pulse voltage, mimicking the process of neurotransmitter release from a presynaptic to a postsynaptic neuron. This phenomenon represents a conductance modulation process where synaptic weight updates occur, with  $\Delta W = (G - G_0)/G_0$ , reflecting changes in synaptic efficacy.<sup>68</sup>

Further illustrated in Figure 7(c), the memristor's response to 50 forward pulses and 50 negative pulses (each 10 ms long) demonstrates a continuous increase in current with each pulse. This behavior models the long-term potentiation (LTP) and long-term depression (LTD) characteristics typical of neural networks,<sup>69,70</sup> which are key processes in learning and memory formation. Figure 7(d) provides a statistical analysis of the synaptic weight updates  $\Delta W = (G - G_0)/G_0$  under different enhancing and inhibiting voltage conditions (50 pulses at 1 V for 1 ms and 50 pulses at −3 V for 10 ms). The results indicate that the synaptic weights of the Ag/CeO<sub>x</sub>/TaO<sub>x</sub>/FTO memristor enhance or suppress progressively with an increasing number of pulses and fluctuate within an acceptable range. This behavior effectively simulates the LTP and LTD dynamics observed in neural networks, showcasing the memristor's potential for applications in neuromorphic computing.<sup>71</sup> This suggests that such devices could be highly beneficial in the emulation of synaptic functions in artificial neural networks, enhancing their ability to mimic human cognitive functions.

The study of spike-timing-dependent plasticity (STDP) in Ag/CeO<sub>x</sub>/TaO<sub>x</sub>/FTO memristors offers valuable insights into the mechanisms of synaptic learning and memory in neural networks.<sup>72</sup> STDP is a form of plasticity where the timing of spikes across synapses significantly influences the synaptic weight, denoted as  $\Delta W$ . This weight changes depending on the temporal difference ( $\Delta t$ ) between the activations of pre- and postsynaptic neurons. Enhancements in synaptic connections occur when presynaptic spikes precede postsynaptic ones, known as the “anterior sequence”. Conversely, synaptic

connections weaken when postsynaptic spikes precede presynaptic ones, referred to as the “posterior sequence”. In the context of memristors, these dynamics are simulated by considering the top electrode as analogous to the presynaptic neuron and the bottom electrode as the postsynaptic neuron. Changes in the memristor conductance reflect changes in synaptic weight, as shown in Figure 7(e). For example, when the potential at the top electrode precedes that at the bottom ( $\Delta t > 0$ ), the synaptic weight increases, and the magnitude of this increase ( $\Delta W$ ) decreases as  $\Delta t$  increases. Conversely, when  $\Delta t < 0$ , the synaptic weight decreases, and  $\Delta W$  similarly decreases with  $\Delta t$ .

The fitting of these changes to a mathematical model resulted in specific parameters that describe the behavior of the synaptic weights over time.<sup>73</sup> The curves of  $\Delta t$  versus  $\Delta W$  were fitted using the following formula:

$$\Delta W = \begin{cases} A_+ e^{-\Delta t/\tau_+} + \Delta W_0, & \Delta t < 0 \\ A_- e^{-\Delta t/\tau_-} + \Delta W_1, & \Delta t \geq 0 \end{cases} \quad (1)$$

The derived parameters, including  $\Delta W_0 = 0.026$ ,  $\Delta W_1 = -0.016$ ,  $A_+ = 1.85$ ,  $A_- = -1.28$ ,  $\tau_+ = 45.4$  ms,  $\tau_- = -54.5$  ms., indicate the model's capability to mimic STDP, with the Ag/CeO<sub>x</sub>/TaO<sub>x</sub>/FTO memristors showing potential for effective simulation of synaptic behaviors in neuromorphic systems.

Paired pulse facilitation (PPF) is recognized as a significant form of synaptic plasticity, characterized by an enhanced postsynaptic response to a second stimulus closely following the first.<sup>74</sup> This response exemplifies the synaptic system's temporary amplification in reaction to consecutive signals. Initially, an electrical signal at the presynaptic neuron triggers an action potential, leading to neurotransmitter release into the synaptic cleft and an increase in intracellular calcium concentration, which is crucial for neurotransmitter release. If a subsequent stimulus rapidly follows, the residual calcium from the first stimulus enhances the effect of the second, resulting in a greater release of neurotransmitters and a correspondingly stronger postsynaptic response, manifesting as PPF.

PPF serves as an adaptive mechanism, allowing neural circuits to temporarily enhance synaptic transmission and adjust synaptic signal gain under specific conditions. This mechanism is vital for encoding processes in learning and memory and provides insight into how neural networks adapt their response patterns to dynamic environmental stimuli. Such understanding is crucial for both functional neuroscience and the development of interventions for neurological disorders.<sup>75</sup>

To explore this phenomenon in an artificial setting, the PPF functionality of the Ag/CeO<sub>x</sub>/TaO<sub>x</sub>/FTO memristor was evaluated. The experimental setup involved applying a pulse voltage of 1 V for 1 ms with a 1 ms interval between pulses, as shown in Figure 7(f). PPF was quantified by the relative increase in current response following the second pulse, defined as  $PPF = (A_2 - A_1)/A_1 \times 100\%$ , where  $A_1$  and  $A_2$  are the current responses to the first and second pulses, respectively. Subsequently, the pulse interval ( $\Delta t$ ) was varied, and a decline in the magnitude of current increase was observed, suggesting a time-dependent decrease in PPF effectiveness, as shown in Figure 7(g). The curves were fitted using the following equation:

$$PPF = C_1 e^{-t/\tau_1} + C_2 e^{-t/\tau_2} \quad (2)$$

The relationship between  $\Delta t$  and PPF was modeled, yielding time constants  $\tau_1 = 1.27$  ms and  $\tau_2 = 5.89$  ms, indicative of the Ag/CeO<sub>x</sub>/TaO<sub>x</sub>/FTO memristor's capability to simulate PPF. These findings underscore the potential of such memristive devices to mimic critical aspects of synaptic behavior, advancing their application in neuromorphic computing.

## CONCLUSIONS

In this study, by introducing the cerium oxide layer in the Ag/CeO<sub>x</sub>/TaO<sub>x</sub>/FTO memristor, we demonstrate a memristor with ultralow switching voltage (0.55 V), high endurance (>1000 cycles), and synaptic functionalities approaching biological fidelity. The CeO<sub>x</sub> layer elevates oxygen vacancy concentration by 23% (XPS) and stabilizes filament formation via interfacial V<sub>o</sub><sup>2+</sup> gradient control. Furthermore, The device achieves linear conductance modulation (nonlinearity  $\alpha=0.92$ ) and biomimetic STDP/PPF. These characteristics demonstrate its potential for constructing neural networks as artificial synapses.

## ASSOCIATED CONTENT

### Data Availability Statement

The data sets generated during and/or analyzed during the current study are available from the corresponding author on request.

## AUTHOR INFORMATION

### Corresponding Author

Hui Zheng – Laboratory for Nanoelectronics and NanoDevices, Department of Electronics Science and Technology, Hangzhou Dianzi University, Hangzhou 310018, China; [orcid.org/0000-0002-5128-6606](https://orcid.org/0000-0002-5128-6606); Email: [zhenghui0551@hdu.edu.cn](mailto:zhenghui0551@hdu.edu.cn)

### Authors

Xinrong Ren – Laboratory for Nanoelectronics and NanoDevices, Department of Electronics Science and Technology, Hangzhou Dianzi University, Hangzhou 310018, China

Yuede Nan – Laboratory for Nanoelectronics and NanoDevices, Department of Electronics Science and Technology, Hangzhou Dianzi University, Hangzhou 310018, China

Xu Chen – Laboratory for Nanoelectronics and NanoDevices, Department of Electronics Science and Technology, Hangzhou Dianzi University, Hangzhou 310018, China

Ruyun Ding – Laboratory for Nanoelectronics and NanoDevices, Department of Electronics Science and Technology, Hangzhou Dianzi University, Hangzhou 310018, China

Complete contact information is available at: <https://pubs.acs.org/10.1021/acsaelm.5c00483>

### Author Contributions

Xinrong Ren, Hui Zheng, Yuede Nan: Writing-original draft. Xinrong Ren, Yuede Nan, Xu Chen: Investigation. Xinrong Ren, Ruyun Ding: Data curation. Hui Zheng: Writing - review and editing.

### Notes

The authors declare no competing financial interest.

## ACKNOWLEDGMENTS

This work is funded by the Fundamental Research Funds for the Provincial Universities of Zhejiang (GK239909299001-402) and the National College Students' innovation and entrepreneurship training program (No. 202410336007).

## REFERENCES

- (1) Yao, P.; Wu, H.; Gao, B.; Tang, J.; Zhang, Q.; Zhang, W.; Yang, J. J.; Qian, H. Fully hardware-implemented memristor convolutional neural network. *Nature* **2020**, 577 (7792), 641–646.
- (2) Zidan, M. A.; Fahmy, H. A. H.; Hussain, M. M.; Salama, K. N. Memristor-based memory: The sneak paths problem and solutions. *Microelectronics Journal* **2013**, 44 (2), 176–183.
- (3) Hwang, B.; Lee, J.-S. Recent Advances in Memory Devices with Hybrid Materials. *Advanced Electronic Materials* **2019**, 5 (1), 1800519.
- (4) Ismail, M.; Rasheed, M.; Mahata, C.; Kang, M.; Kim, S. Nanocrystalline ZnO memristor for neuromorphic computing: Resistive switching and conductance modulation. *J. Alloys Compd.* **2023**, 960, 170846.
- (5) Panda, D.; Hui, Y.-F.; Tseng, T.-Y. J. M. T. E. Diffusion limiting layer induced tantalum oxide based memristor as nociceptor. *Materials Today Electronics* **2023**, 3, 100031.
- (6) Darwish, M. A.; Saafan, S. A.; El-Kony, D.; Salahuddin, N. A. Preparation and investigation of dc conductivity and relative permeability of epoxy/Li-Ni-Zn ferrite composites. *J. Magn. Magn. Mater.* **2015**, 385, 99–106.
- (7) Kim, H.; Sah, M. P.; Yang, C.; Roska, T.; Chua, L. O. Memristor Bridge Synapses. *Proceedings of the IEEE* **2012**, 100 (6), 2061–2070.
- (8) Azghadi, M. R.; Linares-Barranco, B.; Abbott, D.; Leong, P. H. W. A Hybrid CMOS-Memristor Neuromorphic Synapse. *Ieee Transactions on Biomedical Circuits and Systems* **2017**, 11 (2), 434–445.
- (9) Secco, J.; Poggio, M.; Corinto, F. Supervised neural networks with memristor binary synapses. *International Journal of Circuit Theory and Applications* **2018**, 46 (1), 221–233.
- (10) Wei, T.; Lu, Y.; Zhang, F.; Tang, J.; Gao, B.; Yu, P.; Qian, H.; Wu, H. Three-Dimensional Reconstruction of Conductive Filaments in HfO<sub>x</sub>-Based Memristor. *Adv. Mater.* **2023**, 35 (10), 2209925.
- (11) Chen, J.; Xu, J.; Chen, J.; Gao, L.; Yang, C.; Guo, T.; Zhao, Y.; Xiao, Y.; Wang, J.; Li, Y. High-performance memristor based on MoS<sub>2</sub> for reliable biological synapse emulation. *Materials Today Communications* **2022**, 32, 103957.
- (12) Diao, S.; Zhang, G.; Ge, J.; Ma, Z.; Chen, W.; Cao, X.; Lin, H.; Pan, S. Dynamic Ag nanoclusters inside atomically thin SiO<sub>x</sub> enable stochastic memristors for physical unclonable functions. *Ceram. Int.* **2023**, 49 (12), 20901–20906.
- (13) Nan, Y.; Zhang, J.; Pan, Y.; Ren, X.; Zhang, L.; Zheng, H. Regulated resistive switching behaviors of Pt/Ni<sub>0.5</sub>Zn<sub>0.5</sub>Fe<sub>2</sub>O<sub>4</sub>/Pt composite films by oxygen pressure. *Ceram. Int.* **2024**, 50, 16481–16488.
- (14) Luo, J.; Zhao, Z.; Huang, X.; Wu, Y.; Liu, Z.; Wei, A.; Liu, J.; Zhao, Y.; Xiao, Z.; Yang, X. Phase-dependent memristive behaviors in FAPbI<sub>3</sub>-based memristors. *Materials Today Communications* **2022**, 33, 104186.
- (15) Matsukatova, A. N.; Emelyanov, A. V.; Kulagin, V. A.; Vdovichenko, A. Y.; Minnekhanov, A. A.; Demin, V. A. Nano-composite parylene-C memristors with embedded Ag nanoparticles for biomedical data processing. *Org. Electron.* **2022**, 102, 106455.
- (16) Park, K.; Chung, P. H.; Sahu, D. P.; Yoon, T.-S. Interface state-dependent synaptic characteristics of Pt/CeO<sub>2</sub>/Pt memristors controlled by post-deposition annealing. *Materials Science in Semiconductor Processing* **2022**, 147, 106718.
- (17) Ascoli, A.; Tetzlaff, R.; Chua, L. Robust Simulation of a TaO Memristor Model. *Radioengineering* **2015**, 24 (2), 384–392.
- (18) Hwang, H.-G.; Pyo, Y.; Woo, J.-U.; Kim, I.-S.; Kim, S.-W.; Kim, D.-S.; Kim, B.; Jeong, J.; Nahm, S. Engineering synaptic plasticity through the control of oxygen vacancy concentration for the

improvement of learning accuracy in a Ta<sub>2</sub>O<sub>5</sub> memristor. *J. Alloys Compd.* **2022**, 902, 163764.

(19) Kim, K. M.; Yang, J. J.; Strachan, J. P.; Grafals, E. M.; Ge, N.; Melendez, N. D.; Li, Z.; Williams, R. S. Voltage divider effect for the improvement of variability and endurance of TaO<sub>x</sub> memristor. *Sci. Rep.* **2016**, 6, 20085.

(20) Ju, D.; Kim, J. H.; Kim, S. Highly uniform resistive switching characteristics of Ti/TaO<sub>x</sub>/ITO memristor devices for neuromorphic system. *J. Alloys Compd.* **2023**, 961, 170920.

(21) Ha, H.; Pyo, J.; Lee, Y.; Kim, S. Non-Volatile Memory and Synaptic Characteristics of TiN/CeO<sub>x</sub>/Pt RRAM Devices. *Materials* **2022**, 15 (24), 9087.

(22) Yang, C.; Sun, B.; Zhou, G.; Zhao, H.; Zhu, S.; Ke, C.; Zhao, Y.; Wang, H. J. A. A. N. M. Evolution between Volatile and Nonvolatile Resistive Switching Behaviors in Ag/TiO<sub>x</sub>/CeO<sub>y</sub>/F-Doped SnO<sub>2</sub> Nanostructure-Based Memristor Devices for Information Processing Applications. *ACS Appl. Nano Mater.* **2023**, 6 (10), 8857.

(23) Mohanty, S. K.; Panda, D.; Reddy, K. P. K.; Lee, P. T.; Wu, C. H.; Chang, K. M. Uniform resistive switching and highly stable synaptic characteristics of HfO<sub>x</sub> sandwiched TaO<sub>x</sub>-based memristor for neuromorphic system. *Ceram. Int.* **2023**, 49 (11), 16909–16917.

(24) Wang, J.; Xing, H.; Hou, W.; Xu, Y. The role of oxygen vacancies in the performance of LiMn<sub>2</sub>O<sub>4</sub> spinel cathodes for lithium-ion batteries. *Phys. Chem. Chem. Phys.* **2023**, 25 (28), 18903–18914.

(25) Xu, S. G.; Zhang, P.; Zhang, X. W. Design of memristor materials from ordered-vacancy zincblende semiconductors. *Physical Review Materials* **2021**, 5 (2), 024603.

(26) Humbert, V.; El Hage, R.; Krieger, G.; Sanchez-Santolino, G.; Sander, A.; Collin, S.; Trastoy, J.; Briatico, J.; Santamaria, J.; Preziosi, D.; Villegas, J. E. An Oxygen Vacancy Memristor Ruled by Electron Correlations. *Advanced Science* **2022**, 9 (27), 2201753.

(27) Wang, L.-G.; Zhang, W.; Chen, Y.; Cao, Y.-Q.; Li, A.-D.; Wu, D. Synaptic Plasticity and Learning Behaviors Mimicked in Single Inorganic Synapses of Pt/HfO<sub>x</sub>/ZnO<sub>x</sub>/TiN Memristive System. *Nanoscale Res. Lett.* **2017**, 12, 65.

(28) Jung, P.-Y.; Panda, D.; Chandrasekaran, S.; Rajasekaran, S.; Tseng, T.-Y. Enhanced Switching Properties in TaO<sub>x</sub> Memristors Using Diffusion Limiting Layer for Synaptic Learning. *Ieee Journal of the Electron Devices Society* **2020**, 8 (1), 110–115.

(29) Wu, W.; Wu, H.; Gao, B.; Deng, N.; Yu, S.; Qian, H. Improving Analog Switching in HfO<sub>x</sub>-Based Resistive Memory With a Thermal Enhanced Layer. *IEEE Electron Device Letters* **2017**, 38 (8), 1019–1022.

(30) Bousoulas, P.; Michelakaki, I.; Skotadis, E.; Tsigkourakos, M.; Tsoukalas, D. Low-Power Forming Free TiO<sub>2-x</sub>/HfO<sub>2-y</sub>/TiO<sub>2-x</sub> Trilayer RRAM Devices Exhibiting Synaptic Property Characteristics. *Ieee Transactions on Electron Devices* **2017**, 64 (8), 3151–3158.

(31) Kim, K. M.; Zhang, J. M.; Graves, C.; Yang, J. J.; Choi, B. J.; Hwang, C. S.; Li, Z. Y.; Williams, R. S. Low-Power, Self-Rectifying, and Forming-Free Memristor with an Asymmetric Programming Voltage for a High-Density Crossbar Application. *Nano Lett.* **2016**, 16 (11), 6724–6732.

(32) Nishi, Y.; Sasakura, H.; Kimoto, T. Conductance fluctuation in NiO-based resistive switching memory. *J. Appl. Phys.* **2018**, 124 (15), 152134.

(33) Liu, F. N.; Peng, Y.; Liu, Y.; Xiao, W. W.; Hao, Y.; Han, G. Q. Performance improvement of a tunnel junction memristor with amorphous insulator film. *Discover Nano* **2023**, 18 (1), 20.

(34) Marjanovic, N. S.; Vujisic, M. L.; Stankovic, K. D.; Despotovic, D.; Osmokrovic, P. V. Simulated exposure of titanium dioxide memristors to ion beams. *Nuclear Technology & Radiation Protection* **2010**, 25 (2), 120–125.

(35) Fang, Y.; Zhao, C.; Gong, Z.; Wang, S.; Ye, X.; Pan, Q.; Li, G.; Cui, Y.; Yao, Y.; Luo, W. In situ NAP-XPS study of CO<sub>2</sub> and H<sub>2</sub>O adsorption on cerium oxide thin films. *Chem. Phys. Lett.* **2022**, 794, 139496.

(36) Araujo, M. P.; Soares, O. S. G. P.; Fernandes, A. J. S.; Pereira, M. F. R.; Freire, C. Tuning the surface chemistry of graphene flakes:

new strategies for selective oxidation. *Rsc Advances* **2017**, 7 (23), 14290–14301.

(37) Wang, W. X.; Yin, F. F.; Niu, H. S.; Li, Y.; Kim, E. S.; Kim, N. Y. Tantalum pentoxide (Ta<sub>2</sub>O<sub>5</sub> and Ta<sub>2</sub>O<sub>5-x</sub>)-based memristor for photonic in-memory computing application. *Nano Energy* **2023**, 106, 108072.

(38) Pretorius, R.; Harris, J. M.; Nicolet, M. A. J. S. S. E. Reaction of thin metal films with SiO<sub>2</sub> substrates. *Solid-State Electronics* **1978**, 21 (4), 667–675.

(39) Li, R.; Wang, W.; Li, Y.; Gao, S.; Yue, W.; Shen, G. Multi-modulated optoelectronic memristor based on Ga<sub>2</sub>O<sub>3</sub>/MoS<sub>2</sub> heterojunction for bionic synapses and artificial visual system. *Nano Energy* **2023**, 111, 108398.

(40) Huang, D.; Dai, J.; Li, Z.; Wen, X.; Feng, W.; Liu, H. Effect of carbon-based nanomaterials on the wave absorption properties of hollow ZnFe<sub>2</sub>O<sub>4</sub>. *Materials Science and Engineering B-Advanced Functional Solid-State Materials* **2023**, 293, 116462.

(41) Martinez-Aguilar, E.; Hmo'k, H. L.; Siqueiros, J. M.; Lopez-Juarez, R. Effect of single and mixed Bi, Ga doping on the magnetic properties of Y<sub>3</sub>Fe<sub>5</sub>O<sub>12</sub>. *Comput. Mater. Sci.* **2022**, 214, 111752.

(42) Bhattacharjee, N.; Mahalingam, K.; Will-Cole, A.; Wei, Y. Y.; Fedorko, A.; Bowers, C. T.; Page, M.; McConney, M.; Heiman, D.; Sun, N. X. Interface Engineering Enabled Low Temperature Growth of Magnetic Insulator on Topological Insulator. *Advanced Materials Interfaces* **2022**, 9 (35), 2201691.

(43) Cho, Y.; Kim, J.; Kang, M.; Kim, S. Analog Resistive Switching and Artificial Synaptic Behavior of ITO/WO<sub>x</sub>/Ta<sub>N</sub> Memristors. *Materials* **2023**, 16 (4), 1687.

(44) Zhu, Y.-L.; Xue, K.-H.; Cheng, X.-M.; Qiao, C.; Yuan, J.-H.; Li, L.-H.; Miao, X.-S. Uniform and robust TiN/HfO<sub>2</sub>/Pt memristor through interfacial Al-doping engineering. *Appl. Surf. Sci.* **2021**, 550, 149274.

(45) Zhai, S. B.; Gong, J. Q.; Feng, Y. F.; Que, Z. B.; Mao, W. W.; He, X. M.; Xie, Y. N.; Li, X. A.; Chu, L. Multilevel resistive switching in stable all-inorganic n-i-p double perovskite memristor. *Iscience* **2023**, 26 (4), 106461.

(46) Zhou, G. D.; Ji, X. Y.; Li, J.; Zhou, F. C.; Dong, Z. K.; Yan, B. T.; Sun, B.; Wang, W. H.; Hu, X. F.; Song, Q. L.; Wang, L. D.; Duan, S. K. Second-order associative memory circuit hardware implemented by the evolution from battery-like capacitance to resistive switching memory br. *Iscience* **2022**, 25 (10), 105240.

(47) Qin, Q.; Zhang, M. C.; Yao, S. H.; Chen, X. Y.; Han, A. Z.; Chen, Z. Y.; Ma, C. X.; Wang, M.; Chen, X. T.; Wang, Y.; Zhang, Q. Q.; Liu, X. Y.; Hu, E. T.; Wang, L.; Tong, Y. Fabrication and investigation of ferroelectric memristors with various synaptic plasticities. *Chinese Physics B* **2022**, 31 (7), 078502.

(48) Feng, J.; Hu, W.; Zeng, F.; Lin, H.; Li, L.; Yang, B.; Peng, Y.; Wu, D.; Huo, B.; Tang, X. Investigation of physically transient resistive switching memory based on GeO<sub>2</sub> thin films. *Appl. Phys. Lett.* **2020**, 117 (19), 192102.

(49) Ahmad, A.; Collins, R. J. p. s. s. Ohmic and space-charge-limited conduction in lead phthalocyanine thin films. *physica status solidi (a)* **1991**, 123 (1), 201–211.

(50) Yan, Z.; Guo, Y.; Zhang, G.; Liu, J. M. High-Performance Programmable Memory Devices Based on Co-Doped BaTiO<sub>3</sub>. *Adv. Mater.* **2011**, 23 (11), 1351–1355.

(51) Jian, Z. A.; Mohanty, S.; Ahmadi, E. J. A. P. L. Temperature-dependent current-voltage characteristics of β-Ga<sub>2</sub>O<sub>3</sub> trench Schottky barrier diodes. *Applied Phys. Lett.* **2020**, 116 (15), 152104.

(52) Lim, E. W.; Ismail, R. Conduction Mechanism of Valence Change Resistive Switching Memory: A Survey. *Electronics* **2015**, 4 (3), 586–613.

(53) Zhou, P. K.; Lin, X. L.; Yang, H. L.; Chen, B. J.; Li, H. H.; Chen, Z. R.; Zheng, S. T. Natural biomaterial-based memristor bearing protonated polydopamine with enhanced bipolar resistive switching performance and environmental robustness. *J. Alloys Compd.* **2022**, 925, 166783.



- (54) He, B.; He, X.; Liu, G.-Q.; Zhu, C.; Wang, J.-F.; Sun, Z.-G. Memristive and magnetoresistance effects of SnSe<sub>2</sub>. *Acta Physica Sinica* **2020**, 69 (11), 117301.
- (55) Dongale, T.D.; Patil, K.P.; Gaikwad, P.K.; Kamat, R.K. Investigating conduction mechanism and frequency dependency of nanostructured memristor device. *Materials Science in Semiconductor Processing* **2015**, 38, 228–233.
- (56) Pisal Deshmukh, A.; Patil, K.; Barve, K.; Bhawe, T. Transient N-GQDs/PVA nanocomposite thin film for memristor application. *Nanotechnology* **2024**, 35 (26), 265706.
- (57) Wang, J. J.; Pan, X. Q.; Luo, W. B.; Shuai, Y.; Zeng, H. Z.; Xie, Q.; Huang, S. T.; Wu, C. G.; Zhang, W. L. Voltage-programmable negative differential resistance in memristor of single-crystalline lithium niobate thin film. *Appl. Phys. Lett.* **2022**, 120 (3), 032901.
- (58) Hsu, C.-C.; Long, P.-X.; Lin, Y.-S. Enhancement of Resistive Switching Characteristics of Sol-Gel TiO<sub>2</sub> RRAM Using Ag Conductive Bridges. *IEEE Trans. Electron Devices* **2021**, 68 (1), 95.
- (59) Shen, Z.; Zhao, C.; Qi, Y.; Xu, W.; Liu, Y.; Mitrovic, I. Z.; Yang, L.; Zhao, C. Advances of RRAM Devices: Resistive Switching Mechanisms. *Materials and Bionic Synaptic Application*. **2020**, 10 (8), 1437.
- (60) Chung, Y.-L.; Cheng, W.-H.; Jeng, J.-S.; Chen, W.-C.; Jhan, S.-A.; Chen, J.-S. Joint contributions of Ag ions and oxygen vacancies to conducting filament evolution of Ag/TaO<sub>x</sub>/Pt memory device. *J. Appl. Phys.* **2014**, 116 (16), 164502.
- (61) Zhu, Y.-L.; Li, L.-H.; Qiao, C.; Zeng, Y.-T.; Yuan, J.-H.; Cheng, X.-M.; Miao, X.-S. Modulation of oxygen transport by incorporating Sb<sub>2</sub>Te<sub>3</sub> layer in HfO<sub>2</sub>-based memristor. *Appl. Phys. Lett.* **2021**, 119 (19), 193503.
- (62) Liang, H. T.; Ke, C.; Sun, B.; Zhu, S. H.; Wen, Q. F.; Huang, M.; Wang, J. Q.; Zhao, Y. Stable resistive switching behavior of polyvinyl alcohol coating film-based memristor under multiple operating voltages by doping AgNWs. *Colloids and Surfaces a-Physicochemical and Engineering Aspects* **2023**, 675, 132053.
- (63) Chen, L.; Zhou, W. H.; Li, C. D.; Huang, J. J. Forgetting memristors and memristor bridge synapses with long- and short-term memories. *Neurocomputing* **2021**, 456, 126–135.
- (64) Maier, P.; Hartmann, F.; Emmerling, M.; Schneider, C.; Kamp, M.; Höfling, S.; Worschech, L. Electro-Photo-Sensitive Memristor for Neuromorphic and Arithmetic Computing. *Physical Review Applied* **2016**, 5 (5), 054011.
- (65) Hong, Q. H.; Zhao, L.; Wang, X. P. Novel circuit designs of memristor synapse and neuron. *Neurocomputing* **2019**, 330, 11–16.
- (66) Wang, S. P.; He, C. L.; Tang, J.; Yang, R.; Shi, D. X.; Zhang, G. Y. Electronic synapses based on ultrathin quasi-two-dimensional gallium oxide memristor. *Chinese Physics B* **2019**, 28 (1), 017304.
- (67) Huang, Y. C.; Liu, J. X.; Harkin, J.; McDaid, L.; Luo, Y. L. An memristor-based synapse implementation using BCM learning rule. *Neurocomputing* **2021**, 423, 336–342.
- (68) Zhu, X. J.; Du, C.; Jeong, Y.; Lu, W. D. Emulation of synaptic metaplasticity in memristors. *Nanoscale* **2017**, 9 (1), 45–51.
- (69) Yin, K. B.; Li, J. C.; Xiong, Y. W.; Zhu, M. Y.; Tan, Z. Y.; Jin, Z. R. Simulating Synaptic Behaviors through Frequency Modulation in a Capacitor-Memristor Circuit. *Micromachines* **2023**, 14 (11), 2014.
- (70) Lee, D.; Lee, S. J.; Kim, J. H.; Kim, G.; Jung, W. G.; Park, J.; Kang, Y. C.; Kim, Y. H.; Song, M.; Kim, H. S.; Choi, J. W. Multi-ion controllable metal halide ionic structure for selective short- and long-term memorable synaptic devices. *Nano Today* **2024**, 55, 102184.
- (71) Kim, T.; Hu, S.; Kim, J.; Kwak, J. Y.; Park, J.; Lee, S.; Kim, I.; Park, J. K.; Jeong, Y. Spiking Neural Network (SNN) With Memristor Synapses Having Non-linear Weight Update. *Frontiers in Computational Neuroscience* **2021**, 15, 646125.
- (72) Nune, P.; Mandal, S.; Saha, A.; Saha, R. A generic simple model of synaptic memristor with local activity for neuromorphic applications. *Journal of Computational Electronics* **2023**, 22 (2), 612–625.
- (73) Campbell, K. A.; Drake, K. T.; Smith, E. H. B. Pulse Shape and Timing Dependence on the Spike-Timing Dependent Plasticity Response of Ion-Conducting Memristors as Synapses. *Frontiers in Bioengineering and Biotechnology* **2016**, 4, 97.
- (74) Zhou, Z. Y.; Zhao, J. H.; Chen, A. P.; Pei, Y. F.; Xiao, Z. A.; Wang, G.; Chen, J. S.; Fu, G. S.; Yan, X. B. Designing carbon conductive filament memristor devices for memory and electronic synapse applications. *Materials Horizons* **2020**, 7 (4), 1106–1114.
- (75) Huang, J. T.; Saleem, A.; Poh, Y. H.; Tseng, T. Y. HfON-Based Optoelectronic Memristor for Synaptic Computing. *Ieee Transactions on Electron Devices* **2024**, 71 (1), 536–541.